

First-principles re-investigation of bulk WO_3

Hanen Hamdi¹, Ekhard K. H. Salje², Philippe Ghosez¹ and Eric Bousquet¹

¹*Theoretical Materials Physics, Q-MAT, CESAM,*

Université de Liège, B-4000 Sart Tilman, Belgium and

²*Department of Earth Sciences, University of Cambridge,
Downing Street, Cambridge CB2 3EQ, United Kingdom*

(Dated: September 15, 2016)

Using first-principles calculations, we analyze the structural properties of tungsten trioxide WO_3 . Our calculations rely on density functional theory and the use of the B1-WC hybrid functional, which provides very good agreement with experimental data. The hypothetical high-symmetry cubic reference structure combines several ferroelectric and antiferrodistortive (antipolar cation motions, rotations and tilts of oxygen octahedra) structural instabilities. The instability related to antipolar W motions combines with those associated to oxygen rotations and tilts to produce the biggest energy reduction, yielding a $P2_1/c$ ground state. This non-polar $P2_1/c$ phase is only different from the experimentally reported Pc ground state by the absence of a very tiny additional ferroelectric distortion. The calculations performed on a stoichiometric compound so suggest that the low temperature phase of WO_3 is not intrinsically ferroelectric and that the reported ferroelectric character might arise from extrinsic defects such as oxygen vacancies. Independently, we also identify never observed $R3m$ and $R3c$ ferroelectric phases with large polarizations and low energies close to the $P2_1/c$ ground state, which makes WO_3 a potential antiferroelectric material. The relative stability of various phases is discussed in terms of the couplings between different structural distortions, highlighting a very complex interplay involving improper-like couplings up to fourth order in the energy expansion in the cubic phase.

Keywords: WO_3 , ferroelectricity, antiferroelectricity, ferroelectricity, perovskites, first-principle calculations, structural instabilities

I. INTRODUCTION

Tungsten trioxide, WO_3 , has been extensively studied due to its very attractive and rich properties for technological applications. WO_3 and its derivatives H_xWO_3 and WO_{3-x} are electrochromic,¹⁻⁶ thermochromic,^{7,8} and superconducting.⁸⁻¹⁵ It has been envisaged that WO_3 may become one of the best materials for electrochromic applications such as in energy-efficient windows, smart glasses, antiglare automobile rear-view mirrors, sunroofs, displays, or even tunable photonic crystals¹⁶ and to reduce photocorrosion.¹⁷ The wide variety of the underlying electronic instabilities for these properties is mirrored by a multitude of related structural instabilities, which were investigated ever since 1975^{18,19} and refined later.²⁰⁻²⁵

All known WO_3 phases are characterized by very large distortions of the archetypal perovskite structure so that even the notion of octahedra tilts is to be taken with some caution. The WO_6 octahedra are so largely distorted that the variance of W-O distances in any observed structure is far greater than in most other known perovskite structures.²⁶⁻³⁰ In this paper we make the fundamental connection between the electronic and structural structure properties of WO_3 and show that most, if not all, structural instabilities can be derived from a careful analysis of its intrinsic cubic phonon instabilities, despite these large deformation amplitudes.

The structural properties can be summarized as follows: WO_3 shows no proper melt, surface melting of crystalline material occurs at 1746 K. Crystal growth

proceeds typically by sublimation and gas transport at temperatures below 1400K. At the highest temperatures the structure is tetragonal (space group $P4/nmm$) with strong antiferrodistortive (AFD) cation movements so that the WO_6 octahedra are strongly distorted³¹ in an anti-polar pattern. Additional rotational octahedral distortions condense in addition to the initial tetragonal displacements when lowering the temperature. They further reduce the symmetry from tetragonal to orthorhombic, monoclinic, triclinic, and finally to a second monoclinic phase. A structural sequence, which contains phases stabilized by temperature, is given in Fig.1. A monoclinic phase ($P2_1/n$)²² and a triclinic phase $P\bar{1}$ exist at room temperature.^{26,27} At higher temperatures, Vogt²³ et al and Locherer *et al.*²⁰ concluded a transition from $Pbcn$ to the $P4/ncc$ phase and Howard³² observed an intermediate $P2_1/c$ phase. Locherer and Woodward found an additional transition from $P4/ncc$ to $P4/nmm$ near at 980 K to 1200 K. Below room temperature, Salje et al²¹ reported a transition from the triclinic $P\bar{1}$ phase to a polar phase (Pc) with no further transitions down to 5K.

WO_3 occurs (almost) always as oxygen deficient WO_{3-x} with a metal-insulator (MI) transition to a metallic phase for high concentrations of oxygen vacancies or doping with alkali metals. Superconductivity occurs in the metallic phase³³ even if the reduced regions are restricted to nano-scale twin boundaries. Bulk superconductivity in WO_{3-x} was found in a tetragonal phase with space group $P\bar{4}2_1m$.³⁴ (Bi-) polaronic electron transport is a characteristic property of WO_{3-x} .³⁵⁻³⁸

Numerous first-principles studies were performed on

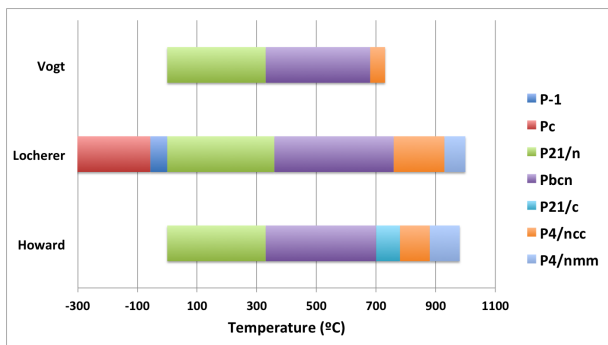


FIG. 1. (Color online) Schematic summary of the temperature phase diagram WO_3 as reported by three main experimental sources (Vogt from Ref. 23, Locherer from Ref. 22 and Howard from Ref. 32).

WO_3 in order to characterize its electronic structure (bulk, thin films and cluster phases^{39–45}) the role of oxygen vacancies,^{46–49} and cation doping.^{50–57} In this paper we focus on the effect of the electronic structure on the structural stabilities and metastabilities of the various phases. We show that the hybrid functional B1-WC is preferable for the study of the electronic and structural properties of WO_3 over previous approaches. In the first section we check the validity of the B1-WC functional against six known crystallographic phases. The sole disagreement exists for the crystallographic ϵ phase (Pc), which yields a higher symmetric $P2_1/c$ structure. In the second section we analyze metastable phases starting from the phonon dispersions of the hypothetical cubic phase, identifying the main phonon instabilities. We then condense various possible combinations of these unstable modes in order to reproduce all experimentally observed structures. This procedure also reveals two new polar phases that are close in energy to the ground-state.

II. COMPUTATIONAL DETAILS

As a preliminary test, we performed calculations on WO_3 using several approaches and codes. We tested the norm-conserving pseudopotentials and projected augmented waves with ABINIT⁵⁸ and VASP^{59,60} codes working within local density approximation⁶¹ (LDA) and different generalized gradient approximations (GGA) including PBE,⁶² PBEsol⁶³ and Wu-Cohen⁶⁴ for the exchange-correlation functional. We also tested the localized orbital approach and the B1-WC⁶⁵ functional as implemented in the CRYSTAL code.⁶⁶

As reported by Wang *et al.*,⁴⁸ we found that PBEsol and Wu-Cohen GGA functionals give good agreement for the structural properties but underestimate the electronic band gap, while the hybrid functionals give good agreement for both the structure and the band gap. Wang *et al.*⁴⁸ investigated B3LYP, PBE0 and HSE06 hybrid functionals and found that the HSE06 gives the

best agreement with experiments. In our study, the B1-WC hybrid functional also gives good results, often better compared with the HSE06 functional. We note that the HSE06 functional was used through the plane wave VASP code, which is highly computer time consuming while the B1-WC with the localized orbital scheme of CRYSTAL is more computationally efficient.

In what follows, we mainly focus on the results obtained with the B1-WC functional and the CRYSTAL code. We have used the all-electron double- ζ basis sets for the oxygen atoms and small core Detlev Figgen pseudo-potentials,⁶⁷ associated with double- ζ valence basis sets for tungsten. We performed full structural relaxations with a convergence criteria on the root-mean-square of the gradient and displacements smaller than 5×10^{-4} hartree/bohr and 5×10^{-4} bohr respectively. The electronic self-consistent calculations were converged until the difference of the total energy was smaller than 10^{-9} Hartree. The phonon frequencies and Born effective charges were computed using frozen phonon numerical differences^{68,69} and the electric polarization through the Berry phase technique.⁷⁰ The integration in the Brillouin zone has been performed with a $8 \times 8 \times 8$ grid of k-points for the cubic unit cell and a $4 \times 4 \times 4$ grid for cells doubled in the three directions with respect to the cubic one.

III. ANALYSIS OF THE EXPERIMENTAL PHASES

Several DFT studies of WO_3 have been performed previously^{41,42,45–48,50–56,71} essentially focusing on the main and most common phases and on the electronic structure analysis with and without oxygen vacancies. A detailed analysis of the complex structural phase diagram of WO_3 is thus missing while a microscopic knowledge of the origin of these different phases would be extremely valuable to understand the unique properties of WO_3 .

In this section we start by characterizing the different phases of WO_3 observed experimentally to validate our approach and we will discuss the possible origin of the Pc phase. We will also analyze the electronic structure of these phases and we will discuss how the B1-WC compares with the previous studies.

A. Structural and crystallographic analysis

In Table I we compare our calculated crystallographic data of the $P4/nmm$, $P4/ncc$, $Pbcn$, $P2_1/n$, $P\bar{1}$ and $P2_1/c$ phases against the experimental measurements. Because the $P2_1/c$ phase is not observed experimentally at low temperature, we compare it with the closely related experimental Pc phase.

Our calculations of the $P4/nmm$ phase are in very good agreement with the observed cell parameters and the atomic positions. The $P4/nmm$ phase consists of highly distorted WO_3 octahedra where the W–O bonds

dimerize in opposite direction along the [110] perovskite direction. This W–O dimerization forms local dipole-moments that are aligned along the [001] direction and anti-aligned along the [110] direction, so that the total dipole-moment cancels. The crystallographic unit cell is elongated along the [001] direction and compressed along the [100] and [010] directions.

The $P4/ncc$ phase shows additional octahedra rotations around the z axis ($a^0a^0c^-$ in the Glazer notation⁷²), which induces a cell doubling along the [001] direction. The calculated c cell parameter and the z component of the atomic positions are in good agreement with experiments while the in-plane displacements are less well reproduced (Tab. I). The calculated a and b cell parameters are smaller than in experiments by 0.1 Å and the deviation from the tetragonal O_2 position are about two times larger than observed. We clearly overestimate the $a^0a^0c^-$ distortions. Note, however, that our calculations ignore thermal effects while experiments were performed at high temperatures.⁷³ A possible comparison would be to extrapolate the experimental data for limited high temperature intervals to 0K but such data are not available for the $P4/ncc$ phase.

The orthorhombic $Pbcn$ phase can be characterized by its additional octahedra rotation about the crystallographic y axis ($a^0b^+a^0$). We find a similar overestimate of the octahedra distortions as for the $P4/ncc$ phase while the calculated cell parameters are underestimated with respect to experiments. We note that the anti-polar distortions along the z axis compares well with experiments for $P4/nmm$, $P4/ncc$ and $Pbcn$.

The $P2_1/n$ structure contains an additional octahedra rotation around the crystallographic x axis ($a^-b^+c^-$). The calculated cell volume is slightly too small (+0.7%, -0.7% and -1.9% for a , b and c cell parameters respectively) and the oxygen motions related to the octahedra tilt are overestimated (Table I).

The $P\bar{1}$ phase is similar to the $P2_1/n$ phase if one replaces the in-phase rotation by an out-of-phase rotation with the pattern $a^-b^-c^-$. The distortions are anisotropic in all three directions, which causes the cell to be triclinic with the angles α , β and γ close to 90°. The calculated a , b and c cell parameters deviate from experiments by +0.4%, -1.1% and -0.8% respectively.

The largest apparent deviation is in the ε (Pc) phase. The Pc phase is related to the $P2_1/c$ phase through an additional polar distortions along the c axis. While relaxing the low temperature Pc phase we observed that the system always relaxes back in to the higher symmetric $P2_1/c$ structure. Wijs *et al* using LDA and GGA exchange correlation functionals⁴² found a similar effect. In Table I we compare our calculated atomic positions and cell parameters of the $P2_1/c$ phase with the experimentally determined Pc phase. The deviations are surprisingly small (+0.2%, -0.2% and -0.5% for a , b and c lattice parameters) and even smaller differences for the atomic positions. To further assess the dynamical stability of the $P2_1/c$ phase with respect to a potential Pc

ground state, we computed the zone-center phonons and did not observe any unstable mode. The lowest polar mode has a frequency of 158 cm^{-1} and is far from being unstable. We also checked whether a soft polar mode can be generated by increasing the cell volume but did not observe any polar instability. We thus follow the argument by Wijs *et al.*⁴² that polarity in the experimental study may be stabilized by the presence of oxygen vacancies or by another extrinsic parameter. Comparing the structural parameters obtained with other hybrid functionals PBE0, B3LYP and HSE06 reported by Wang *et al.*⁴⁶, we find close agreement with a smaller error margin for B1-WC. B1-WC gives a much better agreement for the $P2_1/c$ phase with experimental data than using the three hybrid functionals tested by Wang *et al.*: HSE06, B3LYP and PBE0 with errors of +0.6%, +1.3% and +0.2% on a , +2.1%, +2.5% and +0.6% on b and +0.1%, +3.0%, +1.7% on the c parameter. We notice, however, that the B1-WC often underestimates cell parameters while the three other hybrid functionals overestimate the cell parameters of WO_3 .

B. Electronic structure

In Table II we compare the calculated electronic structures for the hypothetical cubic, $P4/nmm$, $P4/ncc$, $Pbcn$, $P2_1/n$, $P\bar{1}$ and $P2_1/c$ phases and compare them with the experiments and previous DFT calculations using PBE0, HSE06 and B3LYP hybrid functionals and GW. For the $P2_1/n$ and $P\bar{1}$ phases, experimental data coincide with the B1-WC band gaps. The B1-WC results are similar to those obtained with the HSE06 functional while the PBE0 gives a slightly smaller gap energy and B3LYP larger values. The B1-WC band gap is closest to the results of GW calculations, an agreement also observed for the $P2_1/c$ phase.

Comparing the trend of band gaps between the different phases, we find that the band gap increases from the cubic (1.5 eV) to the lower symmetry phases (Table II). This means that both the anti-polar and octahedra tilt distortions increase the band gap of WO_3 . The calculated electronic gap energies is in reasonable agreement with the experimental values for the three low-temperature structures: $E_g = 2.85$ eV for the room temperature monoclinic phase $P2_1/n$, $E_g = 2.98$ eV for the triclinic phase $P\bar{1}$ and $E_g = 3.28$ eV for the monoclinic phase $P2_1/c$. Figure 2 shows the density of states (DOS) of these three phases to demonstrate their similarity.

IV. ORIGIN OF THE WO_3 PHASES

The results presented so far give us confidence that the B1-WC functional reproduces well the experimental measurements so that we can now focus on the structural instabilities of the hypothetical $Pm\bar{3}m$ cubic parent phase and explain how their condensation give rise

TABLE I. Calculated lattice parameters and Wyckoff positions of distorted WO_3 phases fully relaxed with the B1-WC functional. For each phase, we specify the space group and the experimental parameters are reported for comparison

$P4/nmm$							$P\bar{1}$										
Present			Exp. ³²				Present			Exp. ²⁶							
a	b	c	a	b	c		a	b	c	a	b	c					
5.29	5.29	3.93	5.29	5.29	3.92		7.33	7.44	7.61	7.30	7.52	7.67					
x	y	z	x	y	z		α	β	γ	α	β	γ					
0.25	0.25	-0.064	0.25	0.25	-0.066		88.64	91.02	91.01	88.81	90.92	90.93					
W ₁ (2c)	O ₁ (2c)	O ₂ (4d)					x	y	z	x	y	z					
0.25	0.25	0	0	0	0		0.2603	0.0172	0.2826	0.2566	0.0259	0.2850					
0.25	0.25	0.49	0.25	0.25	0.49		0.2540	0.5210	0.2183	0.2502	0.5280	0.2158					
0	0	0	0	0	0		0.2397	0.0228	0.7793	0.2438	0.0313	0.7817					
$P4/ncc$							$P\bar{1}$										
Present			Exp. ³²				Present			Exp. ²⁶							
a	b	c	a	b	c		a	b	c	a	b	c					
5.17	5.17	7.86	5.27	5.27	7.84		7.33	7.44	7.61	7.30	7.52	7.67					
x	y	z	x	y	z		α	β	γ	α	β	γ					
0.25	0.25	0.2849	0.25	0.25	0.2832		88.64	91.02	91.01	88.81	90.92	90.93					
W ₁ (4c)	O ₁ (4c)	O ₂ (8f)					x	y	z	x	y	z					
0.25	0.25	0.0057	0.25	0.25	0.003		0.2603	0.0172	0.2826	0.2566	0.0259	0.2850					
0.057	-0.057	0.25	0.025	-0.025	0.25		0.2540	0.5210	0.2183	0.2502	0.5280	0.2158					
$Pbcn$							$P\bar{1}$										
Present			Exp. ²³				Present			Exp. ²⁶							
a	b	c	a	b	c		a	b	c	a	b	c					
7.28	7.52	7.68	7.33	7.57	7.74		7.33	7.44	7.61	7.30	7.52	7.67					
x	y	z	x	y	z		α	β	γ	α	β	γ					
0.251	0.026	0.28	0.252	0.029	0.283		88.64	91.02	91.01	88.81	90.92	90.93					
W ₁ (3d)	O ₁ (3d)	O ₂ (3d)	O ₃ (3d)				x	y	z	x	y	z					
-0.001	0.043	0.215	-0.002	0.032	0.221		0.2603	0.0172	0.2826	0.2566	0.0259	0.2850					
0.293	0.259	0.259	0.283	0.269	0.259		0.2540	0.5210	0.2183	0.2502	0.5280	0.2158					
0.287	0.010	0.006	0.280	0.013	0.002		0.2397	0.0228	0.7793	0.2438	0.0313	0.7817					
$P2_1/n$							$P2_1/c$										
Present			Exp. ³²				Present			Exp. (Pc) ⁷⁴							
a	b	c	a	b	c		a	b	c	a	b	c					
7.35	7.48	7.54	7.30	7.53	7.69		5.26	5.15	7.62	5.28	5.16	7.66					
α	β	γ	α	β	γ		α	β	γ	α	β	γ					
90	91.31	90	90	90.85	90		90	91.78	90	90	91.75	90					
x	y	z	x	y	z		x	y	z	x	y	z					
0.2720	0.0074	0.2790	0.2528	0.02600	0.28550		-0.0093	-0.0173	0.6843	-0.0099	-0.02	0.6743					
W ₁ (4e)	W ₂ (4e)	O ₁ (4e)	O ₂ (4e)	O ₃ (4e)	O ₄ (4e)	O ₅ (4e)	O ₆ (4e)		W ₁ (2a)	W ₂ (2a)	O ₁ (2a)	O ₂ (2a)	O ₃ (2a)	O ₄ (2a)	O ₅ (2a)	O ₆ (2a)	
0.2270	0.0133	0.7750	0.24970	0.034410	0.78050		0.5011	0.4827	0.7530	0.5	0.4710	0.75					
0.0043	0.0410	0.2165	0.0003	0.0337	0.2122		0.4975	0.5769	-0.0245	0.4920	0.5780	-0.0230					
-0.0056	0.4576	0.2170	-0.0011	0.4632	0.2177		0.2087	0.2891	0.1794	0.2130	0.2890	0.1830					
0.2883	0.2534	0.2924	0.28430	0.25980	0.2852		0.2830	0.7891	0.2580	0.2830	0.7860	0.2590					
0.2029	0.2530	0.7198	0.2080	0.2588	0.73320		0.6999	0.2090	0.1795	0.7050	0.2070	0.1820					
0.2795	0.0385	0.0059	0.28560	0.0410	0.0041		0.7918	0.7090	0.2579	0.7960	0.7110	0.2610					
0.2790	0.4630	-0.0047	0.28410	0.48680	-0.0056		-0.0058	0.0769	0.4630	-0.0058	0.073	0.4616					

TABLE II. Electronic band gap (in eV) of different phases of WO_3 as calculated in the present work with the B1-WC hybrid functional. We compare with the results of previous hybrid functional calculations (PBE0, HSE06 and B3LYP), the GW approach and experiments.

	Ref. cubic	$P4/nmm$	$P4/ncc$	Pcnc	$P2_1/n$	$P\bar{1}$	$P2_1/c$
B1-WC	1.5	2.12	2.15	2.65	2.85	2.98	3.28
GW	40				2.90	3.00	3.30
PBE0	46	2.25	2.28		3.35	3.67	3.67
HSE06	46	1.67	1.71		2.57	2.80	2.94
B3LYB	46	1.89	1.85		2.89	3.13	3.17
Exp 1	39					2.75	
Exp 2	75					3.21	3.25
Exp 3	47	1.75		2.35	2.60		

to the various known phases of WO_3 . This also allows us to identify novel ferroelectric metastable phases. In each case, we analyze the crystallographic structure through a

decomposition of the distortions with respect to the cubic parent phase in terms of symmetry-adapted modes.

A. Unstable modes of the cubic reference

Fig. 3 shows the calculated phonon dispersion curves of hypothetical cubic WO_3 . Two branches of instabilities (imaginary frequencies plotted as negative numbers in Fig.3) coexist in the Brillouin zone.

The first unstable branch has its largest imaginary value at Γ . The Γ unstable mode has the irreducible representation (irrep) Γ_4^- and corresponds to a polar mode. It suggests that the cubic phase of WO_3 is mostly unstable via this polar instability and might be ferroelectric, which we will see later is not exactly the case. The polar instability at Γ propagates toward the X and M points with weak dispersion while it strongly disperses towards

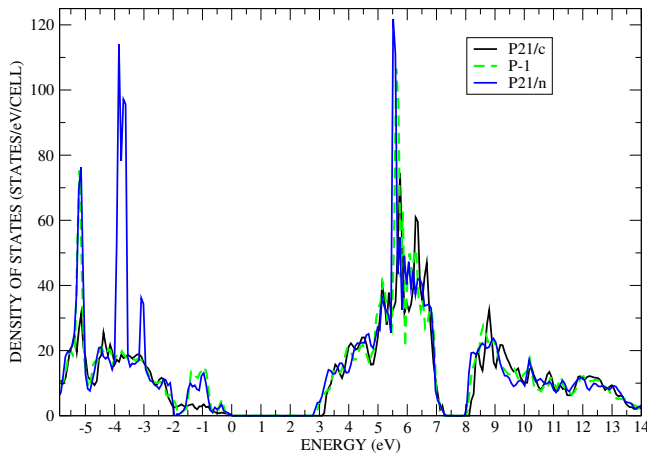


FIG. 2. (Color online) Calculated density of states of the $P\bar{1}$, $P2_1/n$ and $P2_1/c$ phases with the B1-WC functional.

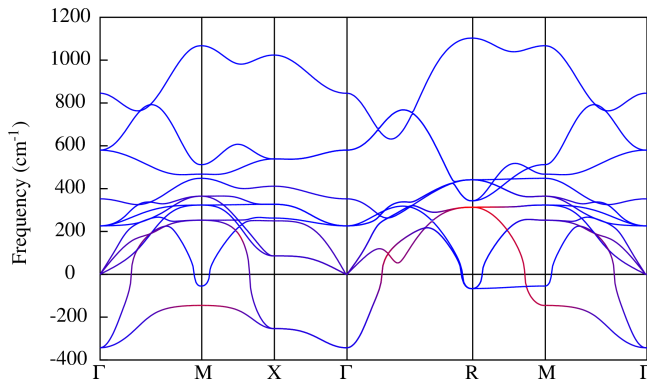


FIG. 3. (Color online) Phonon dispersion curves of cubic WO_3 (negative frequencies refer to imaginary frequencies, *i.e.* to unstable modes). The coordinates of the high symmetry points are as follows: Γ (0,0,0), X ($\frac{1}{2}$, 0, 0), M ($\frac{1}{2}$, $\frac{1}{2}$, 0) and R ($\frac{1}{2}$, $\frac{1}{2}$, $\frac{1}{2}$). Thanks to the *band2eps* postprocessing script of ABINIT,⁵⁸ the color of the bands is assigned to each point through the contribution of each atom type to the corresponding eigenvector: red for the tungsten atom and blue for the oxygens.

the R point. Aside from Γ , the modes of this branch are anti-polar. The dispersion of this unstable branch is very similar to the one reported in BaTiO_3 and corresponds to a ferroelectric instability requiring a chain-like correlation of displacements in real space.⁷⁶

The second branch of unstable modes appears between M and R points with smaller amplitudes and a nearly absent dispersion between these two points. The label of the M and R point unstable phonon modes are M_3^+ and R_4^+ and they correspond to rotations of the oxygen octahedra. The dispersion of this branch is comparable to what is observed for similar modes in SrTiO_3 or PbTiO_3 and linked to a planar character of the correlations of the atomic displacements in real space.⁷⁶

Fig. 4 represents a schematic view of the eigenvectors related to the main instabilities of cubic WO_3 . The polar

mode at Γ (Γ_4^- , $373i$ cm^{-1}) shows motion of W against the O atoms, which is the source of a large electrical polarization. The anti-polar modes at the X (X_5^- , $256i$ cm^{-1}) and M points (M_3^- , $147i$ cm^{-1}) are associated to opposite displacements from unit cell to unit cell along the $[100]$ and $[110]$ directions respectively.⁷⁷ The M_3^+ ($62i$ cm^{-1}) and R_4^+ ($69i$ cm^{-1}) unstable modes correspond to rotations of the oxygen octahedra about the central W atom with consecutive octahedra along the rotation direction moving respectively in the same or opposite directions. Using the Glazer notation,⁷² the M_3^+ mode corresponds to $a^0a^0a^+$ and the R_4^+ mode to $a^0a^0a^-$.

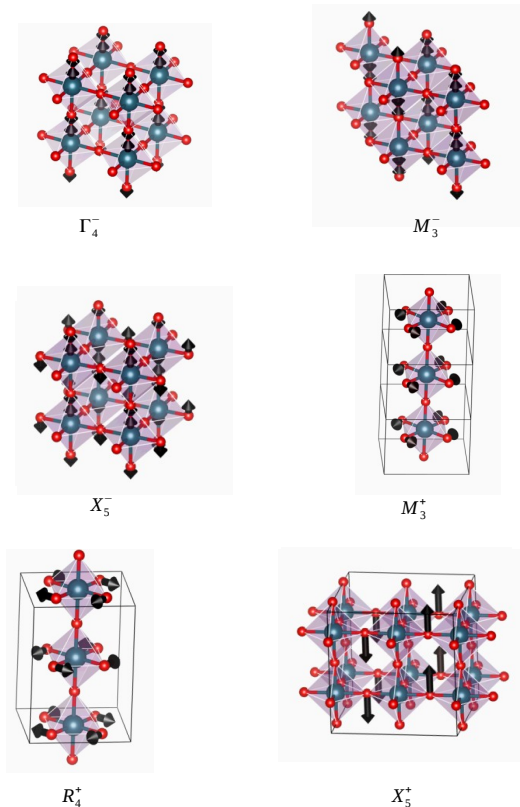


FIG. 4. (Color online) Schematic view of most important modes contributing to the distortions of WO_3 . Small red spheres represent the oxygens and large blue spheres represent the tungsten atoms. All the modes are unstable but the X_5^+ mode, which is discussed in section IV B 4.

B. Condensation and coupling of modes

Starting from the previous unstable modes, we now investigate how their individual and combined condensations in the hypothetical cubic structure give rise to various phases. We then compare their energies and analyze the amplitudes of distortions.

1. Condensation of modes of the unstable polar branch

We first consider the condensation of unstable Γ_4^- , X_5^- and M_3^- modes. Fig. 5 shows the energy gain of the corresponding relaxed phase with respect to the cubic phase. We tested several condensation schemes: (i) condensation of the polar Γ_4^- mode along one ($P4mm$), two ($Amm2$) and three ($R3m$) directions ; (ii) condensation of the X_5^- along one ($Pmma$) and two ($P2_1/m$) directions; (iii) condensation of the M_3^- mode along one direction ($P4/nmm$).

We observe that the energy gain of the polar instabilities is large and that the Γ_4^- polar mode drives a larger gain of energy (red columns in Fig. 5) than the anti-polar X_5^- and M_3^- modes (green columns in Fig. 5). The space group related to the condensation of the M_3^- mode corresponds to the high temperature phase observed experimentally ($P4/nmm$).

Condensation of the Γ_4^- mode along two and three directions produce energy gains larger than its condensation in a single direction so that Γ_4^- mode alone will drive the system polar along the [111] direction with an energy difference between the $Amm2$ and $R3m$ phases of 6 meV. We calculated the polarization amplitude in the three $P4mm$, $Amm2$ and $R3m$ phases using the Berry phase technique and obtain 54, 69 and 69 $\mu\text{C}\cdot\text{cm}^{-2}$. These polarization values are comparable to those observed in robust ferroelectrics such as PbTiO_3 . They can be explained by the opposite motions of W and O atoms, associated with strongly anomalous Born effective charges (11.73 e for W and -8.78/-1.62 e for $\text{O}_{\parallel}/\text{O}_{\perp}$ in good agreement with previous calculations in Ref. 78).

2. Condensation of modes of the oxygen rotation unstable branch

Fig. 5 (blue columns) shows the energy gain given by the condensation of the M_3^+ and R_4^+ modes along one direction ($I4/mbm$ and $I4/mcm$), the R_4^+ mode in three directions ($R\bar{3}c$) and the orthorhombic $Pnma$ phase where the R_4^+ mode is condensed in two directions and the M_3^+ mode in one direction ($a^-a^-c^+$). These distortions lower the energy much less than the polar and antipolar motions. This observation is in line with the modest amplitude of the related phonon instabilities : the energy curvatures at the origin are less negative for the octahedral rotations than for the polar motion. Nevertheless the amplitude of octahedral rotations are 10.7 and 11.7 degrees in $I4/mbm$ and $I4/mcm$, respectively. Such large distortions associated to a weak instability highlight relatively small anharmonicities, which might be explained by the absence of A cation with respect to regular ABO_3 perovskites.⁷⁹

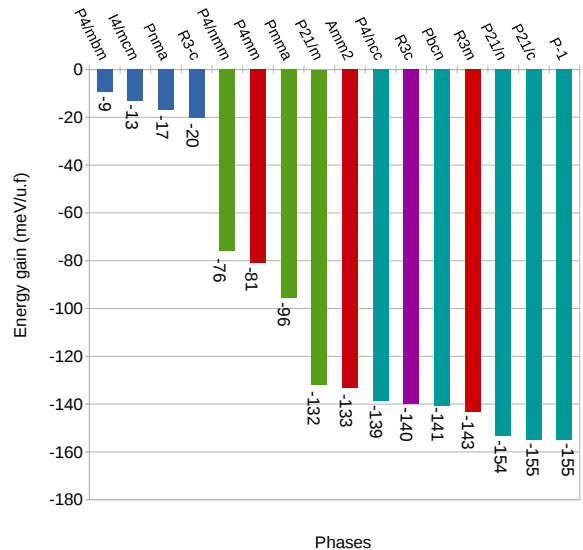


FIG. 5. (Color online) Calculated energy gain (in meV/f.u.) with respect to the cubic phase of different phases of WO_3 . Red columns are the FE phases arising from the condensation of the polar unstable mode, blue columns are the phases arising from the condensation of the oxygens octahedral rotation unstable modes, green columns are the phases arising from the condensation of anti-polar modes, magenta column represents a phase combining FE and anti-polar modes and cyan columns represent phases combining oxygen octahedral rotations and anti-polar modes. For clarity, the exact value of the energy gain is written in each case.

3. Combinations of modes

Beside the $P4/nmm$ phase, none of the previous single irrep mode condensations correspond to observed phases. Thus, we now explore the condensation of combined octahedral rotations and polar/anti-polar modes. We depict in Fig. 5 the energy gain given by the joint condensation of polar and oxygen rotation modes along three directions ($R3c$, in purple color) and of anti-polar and oxygen rotation modes ($P4/ncc$, $Pbcn$, $P2_1/n$, $P2_1/c$ and $P\bar{1}$, in cyan color).

Combining the polar distortion of the low energy $R3m$ phase with additional oxygen rotation modes does not further reduce the energy. Instead, it yields a $R3c$ phase slightly higher in energy but with a slightly amplified polarization of 71 $\mu\text{C}\cdot\text{cm}^{-2}$ and a slightly reduced oxygen rotation (with respect to the $R\bar{3}c$). This emphasizes an unusual competition between these two types of distortions in WO_3 with respect to regular perovskite compounds, where in WO_3 the $R3c$ phase forms a local minimum between the $R\bar{3}c$ and $R3m$ phases.

At the opposite, the mixing of the anti-polar mode M_3^- with oxygen rotation modes can drive larger energy gains so that the ferroelectric $R3m$ phase is not the ground state. This is in agreement with experimental observations where the observed phases at all temperatures con-

tain anti-polar motions. Amongst investigated phases, the $P2_1/c$ phase appears as the most stable but only marginally, as we observe that the $P2_1/n$, $P2_1/c$ and $P\bar{1}$ phases are all extremely close in energy (energy gains of 153, 155 and 155 meV respectively, see Fig. 5). Consequently, within the precision of our calculations, we cannot unambiguously assess which one is the ground state. Nevertheless, as discussed in Section III-A and further exemplified in the next Section, the $P2_1/c$ phase is in excellent agreement with the experimental Pc ground state, except for a tiny polar distortion. Our calculations highlight that, in fact, the $P2_1/n$ and $P\bar{1}$ phases observed at higher temperatures are also extremely close in energy.

We further notice that the ferroelectric $R3m$ phase, although never observed experimentally, is also relatively close in energy to the ground state (about 11 meV/f.u.). Following K. M. Rabe,⁸⁰ the non-polar (or eventually weakly polar in the experimental Pc phase) ground-state of WO_3 combined with an alternative low-energy ferroelectric phase obtained by polar distortions of the same high-symmetry reference structure makes it a potential antiferroelectric compound. Indeed, applying an electric field, it might be possible to open a typical double hysteresis loop from a field-induced first-order transition from the $P2_1/c$ ground state to the $R3m$ polar phase. Estimating the critical electric field required to stabilize the $R3m$ phase from $\mathcal{E}_c \sim \Delta E/\Omega_0 P_s$,⁸¹ where ΔE is the energy difference between the two phases (11.43 meV/f.u.), P_s the spontaneous polarization of the polar phase ($69\mu\text{C}\cdot\text{cm}^{-2}$) and Ω_0 its unit cell volume (55\AA^3), we get the relatively modest value $\mathcal{E}_c \sim 480$ kV/cm. For the polar phase $R3c$ we need to apply a greater electric field $\mathcal{E}_c \sim 638$ kV/cm to stabilize this phase. This allows us to estimate that the critical field has similar value with respect to other antiferroelectric material, $\mathcal{E}_c \sim 470$ kV/cm for ZrO_2 ⁸¹ and $\mathcal{E}_c \sim 239$ kV/cm for PbZrO_3 .⁸² Although this might not be easy to check experimentally on real samples that are typically oxygen deficient and highly conductive, the calculations reveal that stoichiometric WO_3 exhibits all the features of an antiferroelectric compound.

4. Symmetry adapted mode analysis of the distorted phases

To quantify the distortions that appear in the various phases we project the structural distortions onto symmetry adapted modes of the cubic phase using AMPLIMODE software.⁸³ The results in Fig. 6 show the amplitudes of the modes in the fully relaxed phases from the calculations but non-observed experimentally. In Fig. 7 we show the amplitudes of modes in both the fully relaxed and observed phases, which can be compared.

In the following we discuss the competition/cooperation character of the mode distortions. In perovskite oxides, it is established that the oxygen rotations are in competition with the ferroelectric displacements but less attention has been given to

the combinations of other types of mode. Often, this cooperation or competition comes from the biquadratic energy term in the free energy expansion with respect to two order parameters. In WO_3 , we observe that the combination between the Γ_4^- mode and the R_4^+ mode along the [111] direction in the $R3c$ phase has the tendency to reduce the amplitude of the oxygen rotations with respect to the $R\bar{3}c$ phase (the R_4^+ mode is 13% smaller in the $R3c$ phase than in the $R\bar{3}c$ phase, see Fig. 6) while the polar mode is unaffected. As discussed in the previous section, the combination of the Γ_4^- and R_4^+ modes forms a local minimum ($R3c$ phase) of higher energy than the $R3m$ phase. This means that the polar distortions are in competition with the oxygen rotations as reported for perovskite oxides, with the difference that the polar mode amplitude is unaffected and that the $R3c$ phase is locally stable (the system does not relax into the lowest energy $R3m$ phase). The strain can also play an important role,⁸⁴ but when performing the same calculations at fixed cell parameters (fixed to the cubic one), we find that the $R3c$ phase still forms a local minimum of higher energy than the $R3m$ phase. This unusual energy landscape can come from the marginal gain of energy of the oxygen rotations while large amplitude of rotations are present.

On the other hand, the association of the oxygen rotations with the antipolar M_3^- mode is cooperative. When we compare the amplitude of the R_4^+ and M_3^- modes of the $P4/nmm$, $I4/mcm$ and $P4/ncc$ (Fig. 6 and Fig. 7) we find that when both the R_4^+ and M_3^- modes are present together in the $P4/ncc$ phase, their amplitude is slightly higher (4% larger) than when condensed alone ($P4/nmm$ and $I4/mcm$ phases). Their combination, however, drives a sizeable gain of energy: the $P4/ncc$ phase is 63 meV and 126 meV lower in energy than the $P4/nmm$ and the $I4/mcm$ phases, respectively. This means that the combination of the oxygen rotations with the antipolar M_3^- mode is much more cooperative than the combination with the polar mode Γ_4^- .

The $Pbcn$ phase can be understood as a distorted $P4/ncc$ phase with additional M_3^+ oxygen rotations along [010]. The resulting tilt pattern is $a^0b^+c^-$ with a small energy gain of 2 meV with respect to the $P4/ncc$ phase and a reduction of mode amplitudes M_3^- , R_4^+ and M_3^+ (16%, 7% and 22% reduction of the M_3^- , R_4^+ and M_3^+ modes with respect to the phases where they are condensed alone, *i.e.*, $P4/nmm$, $I4/mcm$ and $P4/mbm$, respectively). The M_3^+ mode competes with the R_4^+ and M_3^- modes in the sense their combination reduces their amplitude, but they cooperate to lower the energy of the system.

In the case of the monoclinic $P2_1/n$, $P2_1/c$ and triclinic $P\bar{1}$ phases, the combination of the M_3^- mode with several oxygen rotations ($a^-b^+c^-$ for $P2_1/n$, $a^-a^-c^-$ for $P2_1/c$ and $a^-b^-c^-$ for $P\bar{1}$) lowers the energy of the crystal and with an increase of the mode amplitude with respect to the phases where these modes are condensed independently. For example, the antipolar M_3^- mode has

his amplitude increased by 11%, 10% and 19% in the $P2_1/n$, $P2_1/c$ and $P\bar{1}$ phases respectively. This means that the dominant R_4^+ oxygen rotations cooperate with the antipolar M_3^- mode to promote the ground state of WO_3 .

We note that in the $P4/nmm$, $P4mm$, $Amm2$, $R3m$, $I4/mcm$, $I4/mbm$, $R\bar{3}c$, $P4/ncc$ and $R3c$ phases the mode decomposition shows only the primary modes we have condensed. This is different with the $Pnma$ phase in which a secondary mode X_5^+ appears with a small amplitude in the mode projections while we have condensed only the primary R_4^+ and M_3^+ modes (see Fig. 6). This additional mode appears by improper coupling between the R_4^+ and M_3^+ modes such that the symmetry of the $Pnma$ structure allows the X_5^+ mode to develop even though the X_5^+ mode is not unstable by itself.⁸⁵ Similarly, we observe the apparition of several additional secondary modes in the $Pbcn$, $P2_1/n$, $P2_1/c$ and $P\bar{1}$ phases, which we discuss in the next section.

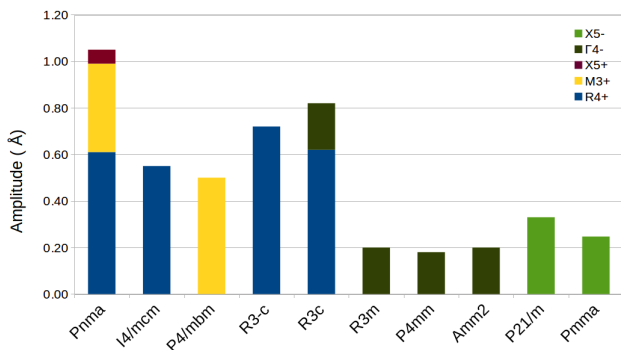


FIG. 6. (Color online) Symmetry adapted mode decomposition of distorted phases of WO_3 explored in our study but not observed experimentally.

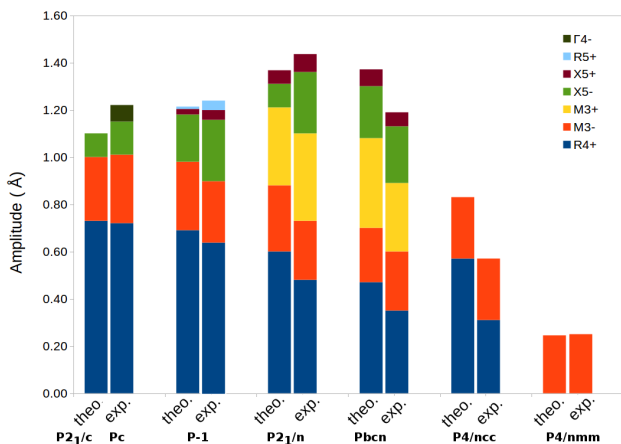


FIG. 7. (Color online) Symmetry adapted mode decomposition of distorted phases WO_3 ; Comparison between experiments and our calculations with the B1-WC functional are shown.

5. Energy invariants and improper couplings

The different phases arise from the condensation of one or several unstable modes (primary modes) of the cubic parent structure but, in some cases, also include the further condensation of stable modes (secondary modes) with significant amplitudes. Often, the appearance of such secondary modes of large amplitude can be traced back in their linear coupling with the primary modes.^{86,87} This can be rationalized from the existence in the energy expansion of the $Pm\bar{3}m$ phase of invariant terms of the form $\gamma Q_s \prod_{i=1}^N Q_p^i$ where Q_s is the amplitude of the secondary mode s and Q_p^i the amplitude of the primary mode i . Depending of the number of primary mode involved, these coupling terms can be bi-linear (pseudo-proper), tri-linear (improper and hybrid-improper), quadri-linear, etc.

To clarify the origin of secondary modes in several low symmetry phases of WO_3 , we restrict ourself here to the search of such multi-linear invariant terms in the energy expansion around its cubic phase by using the INVARIANTS software.⁸⁸ In the last column of Table III we report these linear invariants up to the fourth order obtained for the $Pnma$, $Pbcn$, $P2_1/n$ and $P2_1/c$ phases. The letters represent the mode amplitudes (Q^i) in the directions specified in the third column where the bold letters refer to the primary modes in the structure (Q_p^i) and the normal letters to secondary modes (Q_s^i).

In the $Pnma$ phase, we find that the X_5^+ mode appears through a trilinear coupling with the oxygen rotations modes R_4^+ and M_3^+ (hybrid-improper coupling, **abc** invariant in Table III). This additional hybrid-improper X_5^+ mode is also found in $Pnma$ of ABO_3 perovskites⁸⁹ where the eigenvector corresponds to anti-polar motions of the A cation. In WO_3 the A-cation is absent and X_5^+ corresponds to similar anti-polar motions but of oxygen instead of the A-site (see Fig. 4).

In $Pbcn$ the primary M_3^- mode condenses along z , the R_4^+ mode along z and the M_3^+ mode along y and four additional secondary modes: X_5^- and X_5^+ with a large amplitude and M_5^+ and M_4^+ with a small amplitude as well as an additional component of the M_3^- mode about the x direction. If we restrict ourself to the strongest X_5^- and X_5^+ modes we find that both are coupled with the R_4^+ and M_3^+ modes through a trilinear coupling (hybrid-improper, **abe** and **abf** invariants in Table III) but also through a quadrilinear coupling with the R_4^+ mode and the two components of the M_3^- mode (**adce** and **adcf** invariants in Table III). We can thus explain the appearance of the X_5^+ and X_5^- modes through a trilinear coupling with the oxygen octahedral rotations and the appearance of the second x component of the anti-polar M_3^- mode through a coupling with the secondary X_5^+ and X_5^- modes and the primary R_4^+ mode. The final structure can thus be seen as anti-polar through the M_3^- mode along z with a canting of its direction toward the x axis and through the X_5^- mode along the y direction, the whole distortions being

associated with the $a^-b^+c^-$ pattern of oxygen rotation distortions.

The transition from $Pbcn$ to $P2_1/n$ can be seen as being induced by the condensation of the R_4^+ mode along the remaining direction for the oxygen rotation octahedral distortions to $a^-b^+c^-$. This means that we find the same mode coupling as in the $Pbcn$ phase plus some extra ones due to the additional mode condensation. Because we do not induce a new irrep, the couplings are the same (i.e. trilinear and quadrilinear between the primary R_4^+ , M_3^+ and M_3^- modes and the secondary X_5^- and X_5^+ modes) but in different directions from the $Pbcn$ phase: we observe the X_5^- and X_5^+ modes in two directions instead of one. Other modes also appear in the symmetry adapted mode analysis but with smaller amplitudes (M_4^+ , M_5^- , M_5^+ and M_2^+), which we do not include in the invariant analysis.

$P\bar{1}$ and $P2_1/c$ are very similar in the sense that for both structures we can envisage the condensation of R_4^+ modes in three directions and the M_3^- mode in one direction. The difference is that in the $P2_1/c$ phase the R_4^+ mode is primary with the same amplitude in two directions and a different amplitude in the third direction ($a^-a^-c^-$ where the M_3^- mode is primary in the z direction) while in the $P\bar{1}$ phase the condensation of the R_4^+ mode has different amplitudes in three directions ($a^-b^-c^-$). In $P2_1/c$ the presence of the X_5^- and M_5^- secondary modes can be explained by trilinear coupling with the R_4^+ and M_3^- primary modes (**acd+bcd** and **abe** invariants in Table III) in a similar way as in the $P2_1/n$ phase.

This analysis shows that the low symmetry phases of WO_3 are complex and involve numerous multilinear couplings of modes if one expands the energy about the cubic phase. We note that, amongst possible couplings, the coupling with the secondary X_5^- mode is most important in all low symmetry phases.

Going further, in order to test whether symmetry arguments can lead to the the polar Pc phase using improper-like couplings, we have tested if there exists a coupling with a polar mode at the Γ point. We did not find any couplings with the R_4^+ , M_3^+ or M_3^- modes. We thus conclude that it is not possible to generate polarity in WO_3 in the limit to these primary modes, which are the ones appearing in other experimental phases.

V. CONCLUSION

In this study, we have performed a first-principles study of WO_3 using the B1-WC hybrid exchange-correlation functional and highlighted that, in comparison to various other functionals, it yields the best overall agreement with experiments regarding electronic and structural properties.

Starting from the inspection of the phonon dispersion curves of an hypothetical cubic structure taken as reference, we have identified two main branches of instabilities and characterized various phases arising from the condensation of one or more unstable modes. Although the dominant phonon instability is associated to a zone-center polar mode, we found a non-polar $P2_1/c$ ground state arising from the combination of cooperative anti-polar distortions and oxygen octahedra rotations. This phase is very similar to the experimentally reported polar Pc ground state, except for the absence of a tiny polar distortion. Our calculations does not show however any tendency of the $P2_1/c$ phase to evolve to a Pc phase suggesting that WO_3 is likely not intrinsically ferroelectric. Instead the ferroelectric character might arise from extrinsic defects such as oxygen vacancies. The $P2_1/c$ phase is anti-polar and defects could easily produce a slightly unbalanced anti-dipole structure, yielding a weak net polarization. In this sense, off-stoichiometric WO_3 might be better described as a *ferrielectric* compound.⁹⁰ The ground state is determined by two antiparallel movements of W off-centerings which exactly compensate each other in the $P2_1/c$ phase. The displacements are almost identical in the Pc phase, but the two displacements do not fully compensate each other. We suspect that such weak ferrielectricity can be induced by defects such as oxygen vacancies.

At the level of our calculations, the $P2_1/c$ ground-state is almost degenerated in energy with the $P2_1/n$ and $P\bar{1}$ phases observed at higher temperature. Also, we discovered the existence of a never observed and low-energy ferroelectric $R3m$ phase with a large polarization. Although this might not be of direct interest due to the conductive character of usual off-stoichiometric samples, the proximity with the $P2_1/c$ ground-state of this structurally-unrelated $R3m$ polar phase toward which the system could be switch through a first-order transition under moderate electric fields, makes WO_3 a potential antiferroelectric material. Investigations of the influence of polarons on the WO_3 structures are currently underway.

VI. ACKNOWLEDGEMENTS

We thank Julien Varignon for his helpful guidance with the CRYSTAL code and Emilio Artacho for interesting discussions. H. H., E. B. and Ph. G. acknowledge the Consortium des Equipements de Calcul Intensif (CECI), funded by the FRS-FNRS (Grant 2.5020.11 and and No. 1175545), and the PRACE project TheDeNoMo for computing facilities and the ARC project AIMED for financial support. E. K. H. S. is grateful for support to EPSRC and the Leverhulme trust. H. H. thanks the AVERROES-ERASMUS Mundus project.

Space group	Irrep.	Direction	Subgroup	Amplitudes (\AA)		Linear Invariants
				Calc.	Exp.	
<i>Pnma</i>	\mathbf{R}_4^+	(a , a ,0)	<i>I4/mma</i>	0.61	—	abc
	\mathbf{M}_3^+	(0,0, c)	<i>P4/mbm</i>	0.38	—	
	\mathbf{X}_5^+	(0, a ,0,0,0)	<i>Cmcm</i>	0.06	—	
<i>Pbcn</i>	\mathbf{R}_4^+	(0,0, a)	<i>I4/mcm</i>	0.47	0.35	abe, adce abf, adcf
	\mathbf{M}_3^+	(0, b ,0)	<i>P4/mbm</i>	0.39	0.30	
	\mathbf{M}_3^-	(c ,0, d)	<i>Ibam</i>	0.23	0.25	
	\mathbf{X}_5^-	(0,0, e , -e ,0,0)	<i>Pmma</i>	0.22	0.25	
	\mathbf{X}_5^+	(0,0,0,0, f , f)	<i>Pmma</i>	0.07	0.06	
<i>P2₁/n</i>	\mathbf{R}_4^+	(0, a , b)	<i>C2/m</i>	0.60	0.48	aeg+ bdf ach+aci-bch+ bci acdg- bcef adeh+adei+ bdeh- bdei
	\mathbf{M}_3^+	(c ,0,0)	<i>P4/mbm</i>	0.34	0.37	
	\mathbf{M}_3^-	(0, d , e)	<i>Ibam</i>	0.27	0.25	
	\mathbf{X}_5^-	(f , -f ,0,0, g , g)	<i>Pmmn</i>	0.09	0.26	
	\mathbf{X}_5^+	(0,0, h , i ,0,0)	<i>P2₁/m</i>	0.06	0.08	
<i>P2₁/c</i>	Γ_4^+	(a , -a , -b)	<i>Cm</i>	0	0.067	acd+ bcd
	\mathbf{R}_4^+	(-b , a , -a)	<i>C2/c</i>	0.73	0.72	
	\mathbf{M}_3^-	(c ,0,0)	<i>P4/nmm</i>	0.27	0.3	
	\mathbf{X}_5^-	(0,0,0, -d ,0,0)	<i>Cmcm</i>	0.10	0.14	

TABLE III. Symmetry adapted modes decomposition and linear couplings of modes of the *Pnma*, *Pbcn*, *P2₁/n*, *P2₁/c* and $\bar{P}\bar{1}$ phases. From the left to right columns, we show the mode label (Irrep.) of the symmetry adapted mode, the direction of the mode condensation, the corresponding subgroup, the amplitude of the distortion in the calculated and in the experimental cases (the modes with an amplitude lower than 0.005 \AA are not shown) and the linear coupling invariants of the most relevant modes where the letters correspond to the one given in the direction column (we highlight in bold the primary modes).

- ¹ E. Salje, *Optics Communications* **24**, 231 (1978).
- ² G. A. Niklasson and C. G. Granqvist, *J. Mater. Chem.* **17**, 127 (2007).
- ³ S. K. Deb, *Solar Energy Materials and Solar Cells* **92**, 245 (2008), selected Papers from the Seventh International Meeting on Electrochromism (IME-7)Seventh International Meeting on Electrochromism.
- ⁴ R. Baetens, B. P. Jelle, and A. Gustavsen, *Solar Energy Materials and Solar Cells* **94**, 87 (2010).
- ⁵ S.-H. Lee, R. Deshpande, P. Parilla, K. Jones, B. To, A. Mahan, and A. Dillon, *Advanced Materials* **18**, 763 (2006).
- ⁶ A. Subrahmanyam and A. Karuppasamy, *Solar Energy Materials and Solar Cells* **91**, 266 (2007).
- ⁷ C. Sella, M. Maaza, O. Nemraoui, J. Lafait, N. Renard, and Y. Sampeur, *Surface and Coatings Technology* **98**, 1477 (1998), papers presented at the Fifth International Conference on Plasma Surface Engineering.
- ⁸ Y. Zhao, Z. C. Feng, Y. Liang, and H. W. Sheng, *Applied Physics Letters* **71**, 2227 (1997).
- ⁹ S. K. Deb, *Solar Energy Materials and Solar Cells* **92**, 245 (2008), selected Papers from the Seventh International Meeting on Electrochromism (IME-7)Seventh International Meeting on Electrochromism.
- ¹⁰ A. Aird and E. K. H. Salje, *Journal of Physics: Condensed Matter* **10**, L377 (1998).
- ¹¹ A. Aird, M. C. Domeneghetti, F. Mazzi, V. Tazzoli, and E. K. H. Salje, *Journal of Physics: Condensed Matter* **10**, L569 (1998).
- ¹² E. Salje, *Ferroelectrics* **12**, 215 (1976).
- ¹³ A. Shengelaya, S. Reich, Y. Tsabba, and K. Müller, *The European Physical Journal B - Condensed Matter and Complex Systems* **12**, 13.
- ¹⁴ V. Barzykin and L. P. Gorkov, *Phys. Rev. Lett.* **89**, 227002 (2002).
- ¹⁵ Y. Kim, M. Alexe, and E. K. H. Salje, *Applied Physics Letters* **96**, 032904 (2010).
- ¹⁶ Granqvist C.G, *Solar Energy Materials and Solar Cells* **60**, 201 (2000).
- ¹⁷ Gillaspie Dane T., Tenent Robert C., and Dillon Anne C., *Journal of Materials Chemistry* **20**, 9585 (2010).
- ¹⁸ E. Salje and K. Viswanathan, *Acta Crystallographica Section A* **31**, 356 (1975).
- ¹⁹ E. Salje, *Acta Crystallographica Section A* **31**, 360 (1975).
- ²⁰ K. R. Locherer, I. P. Swainson, and E. K. H. Salje, *Journal of Physics: Condensed Matter* **11**, 4143 (1999).
- ²¹ E. K. H. Salje, S. Rehmman, F. Pobell, D. Morris, K. S. Knight, T. Herrmannsdörfer, and M. T. Dove, *Journal of Physics: Condensed Matter* **9**, 6563 (1997).
- ²² K. R. Locherer, I. P. Swainson, and E. K. H. Salje, *Journal of Physics: Condensed Matter* **11**, 6737 (1999).
- ²³ T. Vogt, P. M. Woodward, and B. A. Hunter, *Journal of Solid State Chemistry* **144**, 209 (1999).
- ²⁴ C. J. Howard, V. Luca, and K. S. Knight, *Journal of Physics: Condensed Matter* **14**, 377 (2002).
- ²⁵ M. Boulova, N. Rosman, P. Bouvier, and G. Lucazeau, *Journal of Physics: Condensed Matter* **14**, 5849 (2002).
- ²⁶ R. Diehl, G. Brandt, and E. Salje, *Acta Crystallographica Section B* **34**, 1105 (1978).
- ²⁷ P. Woodward, A. Sleight, and T. Vogt, *Journal of Physics and Chemistry of Solids* **56**, 1305 (1995).

- ²⁸ P. Woodward, A. Sleight, and T. Vogt, *Journal of Solid State Chemistry* **131**, 9 (1997).
- ²⁹ S. Tanisaki, *Journal of the Physical Society of Japan* **15**, 573 (1960).
- ³⁰ B. O. Loopstra and P. Boldrini, *Acta Crystallographica* **21**, 158 (1966).
- ³¹ W. L. Kehl, R. G. Hay, and D. Wahl, *Journal of Applied Physics* **23**, 212 (1952).
- ³² C. J. Howard, V. Luca, and K. S. Knight, *Journal of Physics: Condensed Matter* **14**, 377 (2002).
- ³³ A. Aird and E. K. H. Salje, *Journal of Physics: Condensed Matter* **10**, L377 (1998).
- ³⁴ A. Aird, M. C. Domeneghetti, F. Mazzi, V. Tazzoli, and E. K. H. Salje, *Journal of Physics: Condensed Matter* **10**, L569 (1998).
- ³⁵ O. Schirmer and E. Salje, *Solid State Communications* **33**, 333 (1980).
- ³⁶ O. F. Schirmer and E. Salje, *Journal of Physics C: Solid State Physics* **13**, L1067 (1980).
- ³⁷ E. Salje, A. Carley, and M. Roberts, *Journal of Solid State Chemistry* **29**, 237 (1979).
- ³⁸ E. Salje and B. Güttler, *Philosophical Magazine Part B* **50**, 607 (1984).
- ³⁹ P. P. González-Borrero, F. Sato, A. N. Medina, M. L. Baesso, A. C. Bento, G. Baldissera, C. Persson, G. A. Niklasson, C. G. Granqvist, and A. Ferreira da Silva, *Applied Physics Letters* **96**, 061909 (2010).
- ⁴⁰ M. B. Johansson, G. Baldissera, I. Valyukh, C. Persson, H. Arwin, G. A. Niklasson, and L. Österlund, *Journal of Physics: Condensed Matter* **25**, 205502 (2013).
- ⁴¹ Y. Ping, D. Rocca, and G. Galli, *Phys. Rev. B* **87**, 165203 (2013).
- ⁴² G. A. de Wijs, P. K. de Boer, R. A. de Groot, and G. Kresse, *Phys. Rev. B* **59**, 2684 (1999).
- ⁴³ A. C. Tsipis and C. A. Tsipis*, *The Journal of Physical Chemistry A* **104**, 859 (2000).
- ⁴⁴ M. G. Stachiotti, F. Corá, C. R. A. Catlow, and C. O. Rodriguez, *Phys. Rev. B* **55**, 7508 (1997).
- ⁴⁵ F. Corá, A. Patel, N. M. Harrison, R. Dovesi, and C. R. A. Catlow, *Journal of the American Chemical Society* **118**, 12174 (1996).
- ⁴⁶ F. Wang, C. D. Valentin, and G. Pacchioni, *The Journal of Physical Chemistry C* **115**, 8345 (2011).
- ⁴⁷ D. B. Migas, V. L. Shaposhnikov, V. N. Rodin, and V. E. Borisenko, *Journal of Applied Physics* **108**, 093713 (2010).
- ⁴⁸ F. Wang, C. Di Valentin, and G. Pacchioni, *Phys. Rev. B* **84**, 073103 (2011).
- ⁴⁹ S. Karazhanov, Y. Zhang, A. Mascarenhas, S. Deb, and L.-W. Wang, *Solid State Ionics* **165**, 43 (2003), fifth International Meeting on Electrochromism.
- ⁵⁰ A. D. Walkingshaw, N. A. Spaldin, and E. Artacho, *Phys. Rev. B* **70**, 165110 (2004).
- ⁵¹ S. Tosoni, C. D. Valentin, and G. Pacchioni, *The Journal of Physical Chemistry C* **118**, 3000 (2014).
- ⁵² A. Hjelm, C. G. Granqvist, and J. M. Wills, *Phys. Rev. B* **54**, 2436 (1996).
- ⁵³ B. Ingham, S. C. Hendy, S. V. Chong, and J. L. Tallon, *Phys. Rev. B* **72**, 075109 (2005).
- ⁵⁴ M. N. Huda, Y. Yan, S.-H. Wei, and M. M. Al-Jassim, *Phys. Rev. B* **80**, 115118 (2009).
- ⁵⁵ F. Corá, M. G. Stachiotti, C. R. A. Catlow, and C. O. Rodriguez, *The Journal of Physical Chemistry B* **101**, 3945 (1997).
- ⁵⁶ M. N. Huda, Y. Yan, C.-Y. Moon, S.-H. Wei, and M. M. Al-Jassim, *Phys. Rev. B* **77**, 195102 (2008).
- ⁵⁷ B. Chen, J. Laverock, L. F. J. Piper, A. R. H. Preston, S. W. Cho, A. DeMasi, K. E. Smith, D. O. Scanlon, G. W. Watson, R. G. Egdell, P.-A. Glans, and J.-H. Guo, *Journal of Physics: Condensed Matter* **25**, 165501 (2013).
- ⁵⁸ X. Gonze and *et al.*, *Computer Physics Communications* **180**, 2582 (2009).
- ⁵⁹ G. Kresse and J. Furthmüller, *Phys. Rev. B* **54**, 11169 (1996).
- ⁶⁰ G. Kresse and D. Joubert, *Phys. Rev. B* **59**, 1758 (1999).
- ⁶¹ M. Teter, *Phys. Rev. B* **48**, 5031 (1993).
- ⁶² J. P. Perdew, K. Burke, and M. Ernzerhof, *Phys. Rev. Lett.* **77**, 3865 (1996).
- ⁶³ J. P. Perdew, A. Ruzsinszky, G. I. Csonka, O. A. Vydrov, G. E. Scuseria, L. A. Constantin, X. Zhou, and K. Burke, *Phys. Rev. Lett.* **100**, 136406 (2008).
- ⁶⁴ Z. Wu and R. E. Cohen, *Phys. Rev. B* **73**, 235116 (2006).
- ⁶⁵ D. I. Bilc, R. Orlando, R. Shaltaf, G.-M. Rignanese, J. Íñiguez, and P. Ghosez, *Phys. Rev. B* **77**, 165107 (2008).
- ⁶⁶ M. Causà, R. Dovesi, C. Pisani, R. Colle, and A. Fortunelli, *Phys. Rev. B* **36**, 891 (1987).
- ⁶⁷ D. Figgen, K. A. Peterson, M. Dolg, and H. Stoll, *The Journal of Chemical Physics* **130**, 164108 (2009).
- ⁶⁸ F. Pascale, C. M. Zicovich-Wilson, F. López Gejo, B. Civaleri, R. Orlando, and R. Dovesi, *Journal of Computational Chemistry* **25**, 888 (2004).
- ⁶⁹ C. M. Zicovich-Wilson, F. Pascale, C. Roetti, V. R. Saunders, R. Orlando, and R. Dovesi, *Journal of Computational Chemistry* **25**, 1873 (2004).
- ⁷⁰ R. D. King-Smith and D. Vanderbilt, *Phys. Rev. B* **47**, 1651 (1993).
- ⁷¹ R. Chatten, A. V. Chadwick, A. Rougier, and P. J. D. Lindan, *The Journal of Physical Chemistry B* **109**, 3146 (2005).
- ⁷² A. M. Glazer, *Acta Cryst. B* **28**, 3384 (1972).
- ⁷³ W. Cochran, *Structural Phase Transitions and Soft Modes*, edited by E. J. Samuelsen, E. Andersen, and J. Feder, Proceedings of the NATO Advanced Study Institute (Universitetsforlaget, 1971) p. 1.
- ⁷⁴ E. K. H. Salje, S. Rehmman, F. Pobell, D. Morris, K. S. Knight, T. Herrmannsdörfer, and M. T. Dove, *Journal of Physics: Condensed Matter* **9**, 6563 (1997).
- ⁷⁵ H. Zheng, J. Z. Ou, M. S. Strano, R. B. Kaner, A. Mitchell, and K. Kalantar-zadeh, *Advanced Functional Materials* **21**, 2175 (2011).
- ⁷⁶ P. Ghosez, E. Cockayne, U. V. Waghmare, and K. M. Rabe, *Phys. Rev. B* **60**, 836 (1999).
- ⁷⁷ In the cubic cell, the [100], [010] and [001] directions are degenerate. The same applies for the [110], [101] and [011] directions.
- ⁷⁸ F. Detraux, P. Ghosez, and X. Gonze, *Phys. Rev. B* **56**, 983 (1997).
- ⁷⁹ N. A. Benedek and C. J. Fennie, *The Journal of Physical Chemistry C* **117**, 13339 (2013).
- ⁸⁰ K. M. Rabe, "Antiferroelectricity in Oxides: A Reexamination," in *Functional Metal Oxides* (Wiley-VCH Verlag GmbH and Co. KGaA, 2013) pp. 221–244.
- ⁸¹ S. E. Reyes-Lillo, K. F. Garrity, and K. M. Rabe, *Phys. Rev. B* **90**, 140103 (2014).
- ⁸² Value calculated from the energies and polarization reported for the *R3m* and *Pbam* phase by S. Amisi in his PhD thesis.

- ⁸³ D. Orobengoa, C. Capillas, M. I. Aroyo, and J. M. Perez-Mato, *Journal of Applied Crystallography* **42**, 820 (2009).
- ⁸⁴ The volume of the cubic, $R\bar{3}c$, $R3m$ and $R3c$ phases are 54.01\AA^3 , 50.89\AA^3 , 55.35\AA^3 , 52.71\AA^3 .
- ⁸⁵ J. Young, A. Stroppa, S. Picozzi, and J. M. Rondinelli, *Journal of Physics: Condensed Matter* **27**, 283202 (2015).
- ⁸⁶ M. G. P. Bousquet E, Dawber, *Nature* **452**, 732 (2008).
- ⁸⁷ N. A. Benedek, J. M. Rondinelli, H. Djani, P. Ghosez, and P. Lightfoot, *Dalton Trans.* **44**, 10543 (2015).
- ⁸⁸ D. M. Hatch and H. T. Stokes, *Journal of Applied Crystallography* **36**, 951 (2003).
- ⁸⁹ N. A. Benedek, A. T. Mulder, and C. J. Fennie, *Journal of Solid State Chemistry* **195**, 11 (2012).
- ⁹⁰ C. F. Pulvari, *Phys. Rev.* **120**, 1670 (1960).